Available online at www.sciencedirect.com

Manufacturing Letters

Manufacturing Letters 35 (2023) 549–556

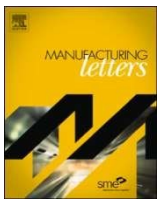

51st SME North American Manufacturing Research Conference (NAMRC 51, 2023)

Hybrid manufacturing by additive friction stir deposition, metrology, CNC machining, and microstructure analysis

Joshua Kincaid[a], Ross Zameroski[a], Elijah Charles[a], Timothy No[b], John Bohling[a], Brett Compton[a], and Tony Schmitz[a,b*]

[a]Mechanical, Aerospace, and Biomedical Engineering Department, University of Tennessee, Knoxville, 1512 Middle Drive, Knoxville, TN, 37996, USA
[b]Manufacturing Demonstration Facility, Oak Ridge National Laboratory, 2350 Cherehala Blvd, Knoxville, TN, 37932, USA

* Corresponding author. Tel.: +1-865-974-6141; E-mail address: tony.schmitz@utk.edu

Abstract

Aerospace flight panels must provide high strength with low mass. For aluminum panels, it is common practice to begin with a wrought plate and remove the majority of the material to attain the desired structure, comprising a thinner plate with the desired pattern of reinforcement ribs. As an alternative, this study implements hybrid manufacturing, where aluminum is first deposited on a baseplate only at the rib locations using additive friction stir deposition (AFSD). Structured light scanning is then used to measure the printed geometry. This geometry is finally used as the stock model for computer numerical control (CNC) machining. This paper details the hybrid manufacturing process that consists of: AFSD to print the preform, structured light scanning to generate the stock model and tool path, three-axis CNC machining, and post-process measurements for part geometry and microstructure.

Peer-review under responsibility of the Scientific Committee of the NAMRI/SME.
Keywords: Hybrid manufacturing, additive friction stir deposition, structured light scanning, machining

1. Introduction

Metal additive manufacturing (AM) includes beam-based technologies, such as powder bed fusion and directed energy deposition, as well as wire arc AM. For these processes, the metal powder or wire is melted using a high intensity heat source and deposited in a layer-by-layer fashion. The gross part geometry is dictated by the computer model fed to the printer, while the microstructure is established during the subsequent solidification and cooling, ultimately dictated by the local temperature gradient and cooling rate [1]. An alternative nonbeam-based, solid-state additive process is provided by additive friction stir deposition (AFSD) [2-5]. In this case, no melting occurs, and the geometry and microstructure are defined by the kinetic energy introduced by the AFSD process. In this sense, AFSD microstructure depends on thermomechanical, rather than solidification, mechanisms. Research efforts have included the study of microstructure and its relationship to mechanical properties and operation parameters [6-15]. Deposition materials have included aluminum, magnesium, copper, and steel alloys [16-20], for example. Repair and cladding [21-24], effect of alloy temper [25], fatigue behavior [26], process modeling [27], and force/temperature control [28] have also been examined in the literature.

The AFSD process is described in Fig. 1. The feedstock is a square metal rod (e.g., wrought material). It is forced through the rotating spindle against the baseplate to generate frictional heat, which softens the feedstock sufficiently to cause plastic flow and, ideally, a metallurgical bond with the existing material. The printed material is constrained axially by the gap between the rotating tool and baseplate (approximately 2.5

Peer-review under responsibility of the Scientific Committee of the NAMRI/SME.

mm). In the lateral direction, there is only friction between the plastically flowing material and the tool (on the top) and baseplate (on the bottom). For this reason, flash can occur at the outer portions of the layer. The tool is translated parallel to the base plate with a selected feed rate to print the layer. For subsequent layers, material is deposited on the previous layer so the microstructure for the previous layer is affected by the plastic deposition from the new layer.

The intent of this paper is to combine AFSD with metrology to identify a work coordinate system and computer numerically controlled (CNC) machining to produce the final geometry and surface finish. The ability to meet the designer's intent for geometry and finish is essential when applying AM processes to produce preforms. A persistent challenge is transferring the coordinate system from the AM to machining processes to ensure that the design is captured within the preform and the machining tool paths are selected to reveal this geometry. This paper provides a case study that demonstrates each step.

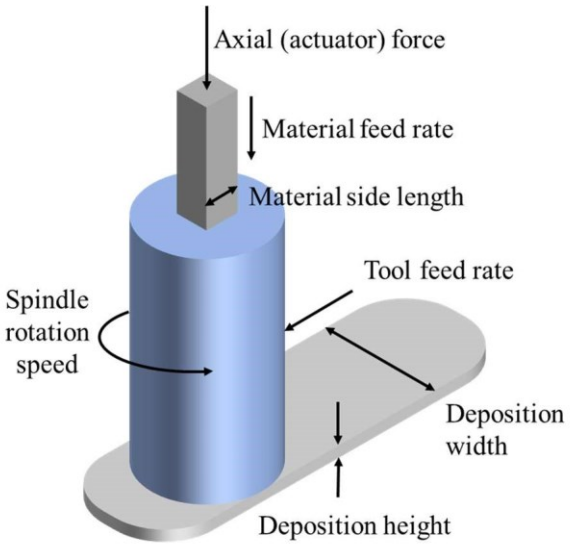

Fig. 1. AFSD description.

2. Hybrid manufacturing steps

To approximate an aerospace flight panel, a ribbed structure with a center hole and boss was designed; see Fig. 2 (left panel), where the ribs are 12.7 mm wide and 10.2 mm tall. The preform was fabricated using a MELD Manufacturing L3 machine to deposit 6061-T6 aluminum square rod with a side length of 9.5 mm onto a 6061-T6 aluminum baseplate. To enable deposition, the AFSD tool paths were generated. These included four overlapping C-shaped paths and a central cylinder that were printed in five layers. The total thickness of the five-layer deposition was 12.7 mm. The preform is displayed in Fig. 2 (the top panel shows the dimension) and the operating parameters are provided in Table 1. In this table, start and final spindle speeds are identified for each layer. These indicate the spindle speeds at the beginning and end of each path. Because heat is generated by both friction and plastic deformation, the temperature increases throughout the path which, subsequently, decreases the yield strength of the wrought stock being deposited. To maintain an approximately constant spindle torque throughout each path, the spindle speed was decreased manually to reduce the heat input.

Table 1. AFSD operating parameters.

Layer	Start spindle speed (rpm)	Final spindle speed (rpm)	Tool feed rate (mm/min)	Material feed rate (mm/min)
1	300	275	102	152
2	300	275	102	152
3	275	275	152	168
4	275	250	142	183
5	275	225	142	198

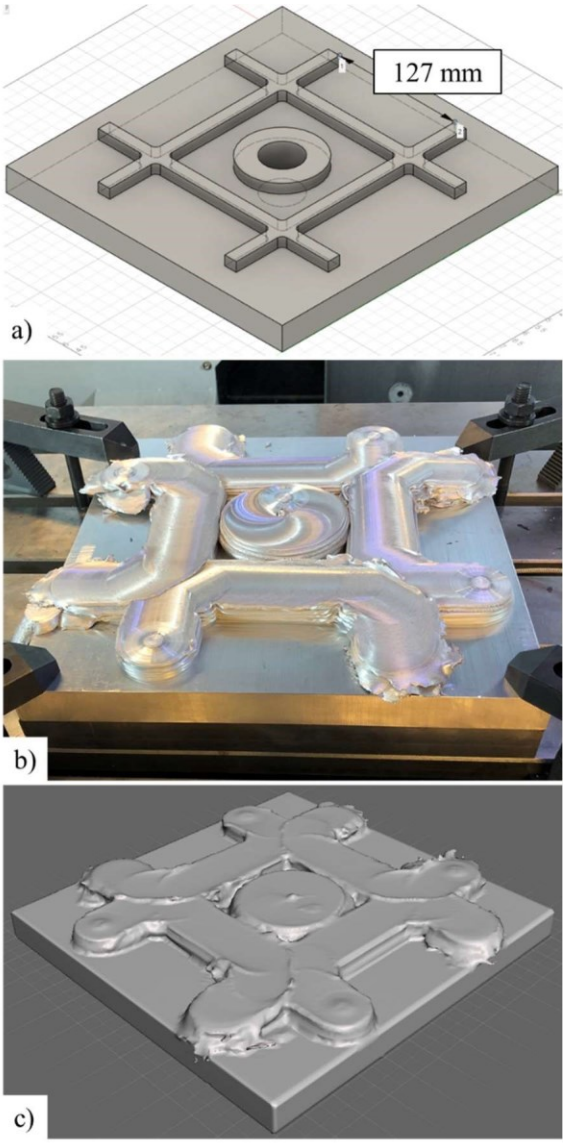

Fig. 2. (a) CAD model of panel. (b) 6061 aluminum preform. (c) Scanned preform model.

The printed preform was measured using a GOM ATOS Q structured light scanner. The scan model was imported into computer aided manufacturing (CAM) software, where it was used as the stock model for toolpath generation. The scan model was aligned with the computer aided design (CAD) model of the ribbed aerospace panel and the coordinate system was assigned using the corner of the baseplate; see Fig. 2 (c). This

approach enabled the tool paths to be generated using the preform and to ensure that the CAD model was contained within this volume. When the part was transitioned to the CNC machining center, the coordinate system was conveniently identified using the touch probe (located in the machine spindle) and standard probing cycles. Once the origin and axes were identified, a coordinate rotation was completed in the CNC part program to align the machining axes to the part axes established in the CAM program. This also eliminated a lengthy stock alignment procedure on the machine table. It was simply placed in approximately the correct orientation (i.e., the preform x axis was nominally aligned with the machine x axis) and then the probing cycle was performed to complete the final alignment through the coordinate rotation.

To select optimal machining parameters, the frequency response functions (FRFs) of each cutting tool were measured using impact testing. Here, a modal hammer (PCB model 086C04) was used to excite the tool tip and the response was measured by a low-mass accelerometer (PCB model 352C23). The FRFs were used to generate stability maps, which enabled the selection of optimal, stable machining parameters [29-30].

Once the machining parameters and toolpaths were selected, the preform was clamped to the table of a Haas VF-4 three-axis CNC milling machine. As noted, the part was then probed with the machine's touch trigger probe to locate the part and align the machine coordinate system with the CAM coordinate system using a coordinate rotation [31-33]. Facing, contour milling, and boring operations were all implemented to create the ribbed structure with a hole and boss in the center. The machining operations are summarized in Table 2 and the CAM toolpaths are displayed in Fig. 3.

Table 2. CNC milling operations and parameters.

Operation	Tool	Spindle speed (rpm)	Feed (mm/min)
1. Face the top surface	76.2 mm diameter, 8 insert facemill	5000	2032
2. Rough contour inner pocket	19.05 mm diameter, 3 flute endmill	7000	1600.2
3. Finish contour inner pocket	6.35 mm diameter, 3 flute endmill	7700	320.0
4. Miller center hole	19.05 mm diameter, 3 flute endmill	7000	1600.2
5. Rough contour outer profile	19.05 mm diameter, 3 flute endmill	7000	1600.2
6. Finish contour outer profile	19.05 mm diameter, 3 flute endmill	7700	320.0

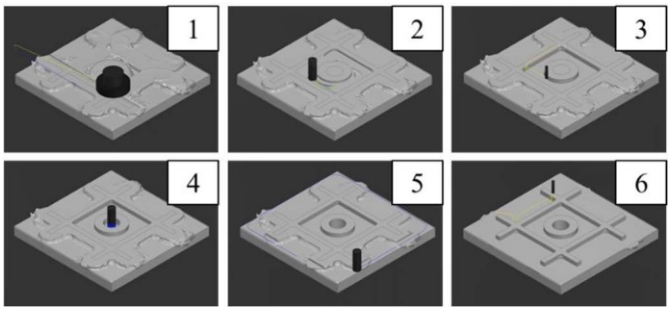

Fig. 3. CNC milling operations from Table 2.

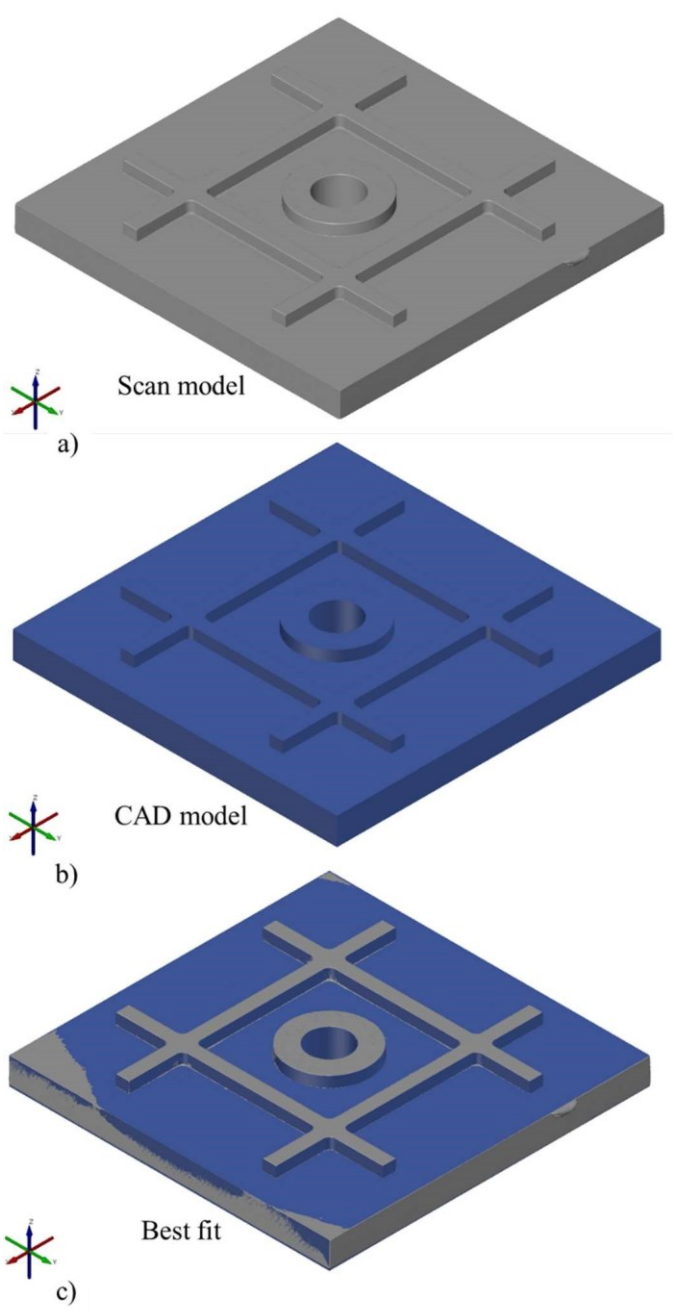

Fig. 4. Comparison of (a) scan model and (b) CAD model using (c) best fit model to determine part errors.

starting volume would have been 3539 cm . In comparison, the preform volume (i.e., the baseplate and printed material) was 3163 cm^3. This represents a material savings of 376 cm^3, or 10.6%, by the hybrid approach. Note that the baseplate comprised 2360 cm^3 of this total volume. Neglecting the baseplate, the "top" wrought volume that contained the ribs and boss was 1180 cm^3 and the printed volume was 804 cm^3. The 376 cm^3 volume savings is now 31.9% of the "top" wrought volume. If machining from the full wrought plate, the amount of material to be removed would have been 1090 cm^3 to obtain the final geometry. Machining the printed preform, on the other hand, required 714 cm^3 to be removed. The difference is again 376 cm^3 for a reduction in material removal volume of 34.5%.

To quantify the geometric fidelity of the machined part, measurements were completed using the structured light scanner [34]. The scan results were compared to the CAD model by creating a best fit alignment and observing the differences; see Fig. 4. The alignment showed a maximum deviation of 0.25 mm from the CAD model; see Fig. 5, where red indicates extra material and blue less material than desired. Higher accuracy is generally expected for machining components, so future work is necessary. One potential cause of these deviations is the release of internal stresses during the machining process. In follow-on testing, measurements will be performed before deposition, after deposition, and after machining to record any part distortion.

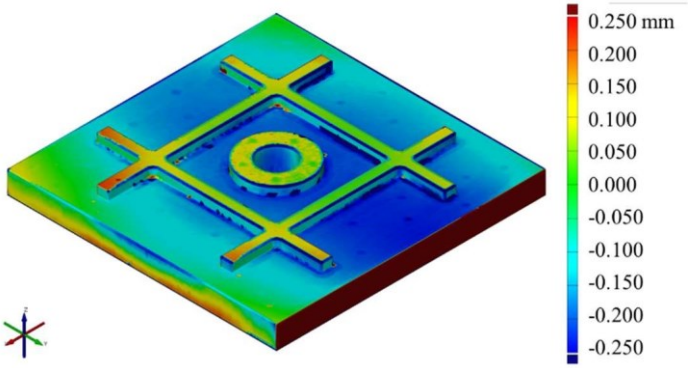

Fig. 5. Difference map between CAD and scan models.

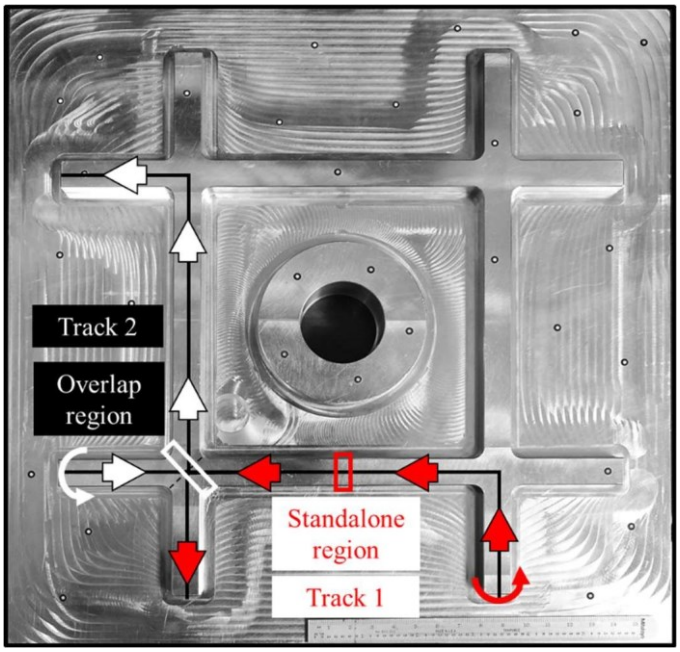

Fig. 6. Standalone (track 1) and overlap (tracks 1 and 2) regions for microstructure evaluation. The dots on the part are targets for structured light scanning.

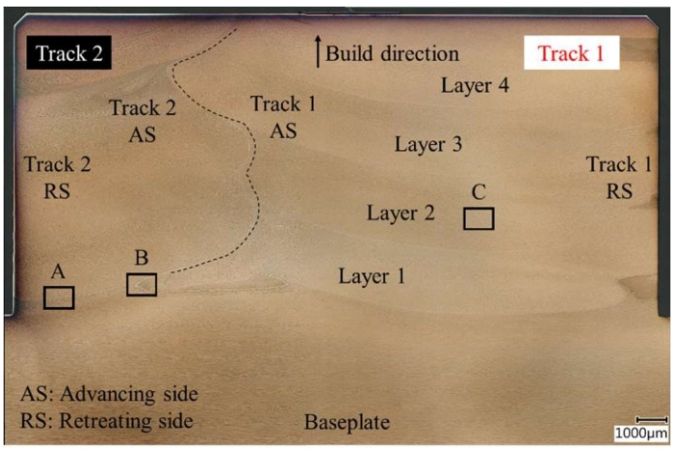

3. Results and discussion

Each step in the hybrid manufacturing process was completed with the expected results. The AFSD toolpaths deposited material in the desired locations on the baseplate. The structured light scan provided a stock model for the CAM software that was used to set a coordinate system and define the toolpaths required to remove the excess material. Stable machining conditions were observed using the optimized parameters obtained from tap testing. In summary, the structured light scanning strategy to provide a CAM stock model and local coordinate system was successfully implemented.

One advantage of the hybrid manufacturing approach is reduced material use and removal (by machining). If the part had been machined from wrought plate stock, the required

Finally, sections were cut from the machined part by water jet to characterize the as-deposited microstructure obtained from the AFSD process. Two sections were studied. These included the overlap region of two C-shaped paths (labeled tracks 1 and 2 in Fig. 6) and a standalone region from the middle of track 1. In Fig. 6, track 1 (red arrows) was deposited first and track 2 (white arrows) was deposited second; the circular arrows indicate the tool rotation direction for each track. The overlap sample (white box) extended across the full width of the overlap region between the two tracks and was oriented normal to the overlap interface. The standalone sample (red box) extended across the width of the track 1 and was oriented normal to the tool feed direction. Both samples were polished and then etched with Weck's reagent for optical microscopy.

The etched cross section of the overlap region is displayed in Fig. 7, where the upper boundary within the image identifies the cross-sectional geometry of the machined rib and the baseplate location is seen as the horizontal intersection. The baseplate region (at the bottom), track 1, and track 2 are individually labeled. In addition, the build direction (i.e., bottom to top layers) and the advancing side (AS) and retreating side (RS) of the deposition are labeled. The advancing side occurs where the peripheral velocity of the rotating tool adds to the tool feed rate, while the retreating side occurs where the peripheral velocity is opposite the tool's feed direction. In Fig. 7, three zones (A, B, and C) are highlighted for higher magnification images and the boundary between tracks 1 and 2 is shown as a dashed line as a guide to the eye.

Fig. 7. Overlap region (tracks 1 and 2) microstructure.

Optical micrographs for zones A, B, and C, as well as the wrought baseplate are shown in Figs. 8-11 for the overlap region between tracks 1 and 2. In each figure, the top image shows a lower magnification and the bottom image shows a higher magnification of the microstructure for each zone. It is observed that the baseplate microstructure (Fig. 8) exhibits elongated features in the horizontal direction due to the rolling operation used to form the plate. The interface between the deposition and baseplate is seen at location A, where the baseplate microstructure has clearly been modified by the deposition process. At location B, a wedge-shaped feature is seen due to the interaction of track 2 and baseplate. Location C shows a uniform, fine grain microstructure in the deposited material due to the severe plastic deformation for the AFSD process.

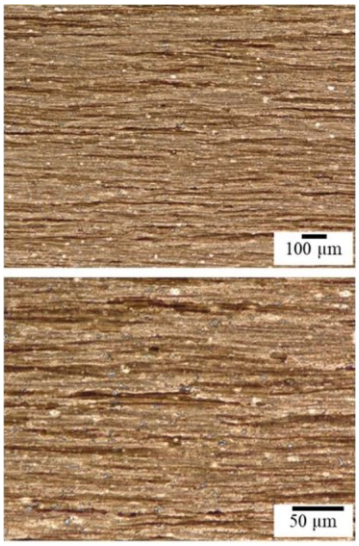

Fig. 8. Individual images for zones in overlap region (tracks 1 and 2): baseplate.

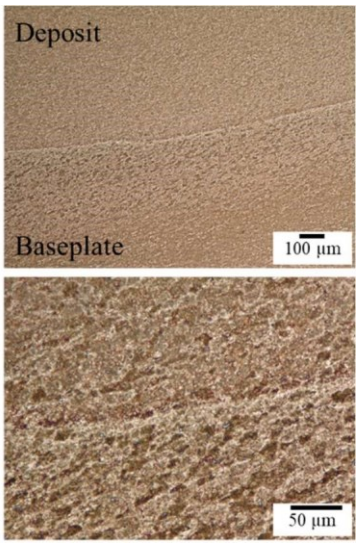

Fig. 9. Individual images for zones in overlap region (tracks 1 and 2): location A, track 2 interface from Fig. 7.

The etched cross section of the standalone (track 1) region is shown in Fig. 12. In this figure, the baseplate region, deposit region, and advancing and retreating sides are labeled; the tool feed direction proceeded out of the image plane during deposition. Optical micrographs for zones A, B, and C, as well as the wrought baseplate are shown in Figs. 13-16. The interface between the deposition and baseplate is shown for location A, where the baseplate microstructure is distinctly different before and after deposition. At location B, a wedgeshaped feature is again seen at the baseplate-deposit interface. Location C shows a uniform, fine grain microstructure for the deposited material. Further characterization of the microstructural changes in the base plate, interface features observed in both regions, and hardness properties will be conducted to understand the effect on behavior of the final part.

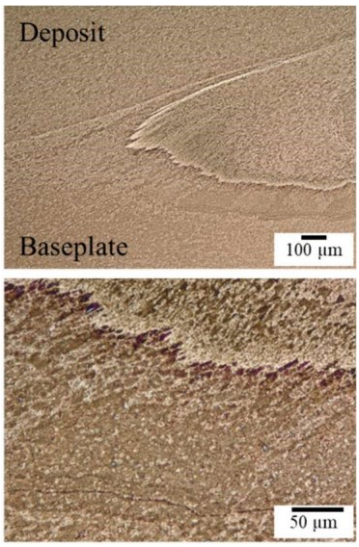

Fig. 10. Individual images for zones in overlap region (tracks 1 and 2): location B, track 2 interface from Fig. 7.

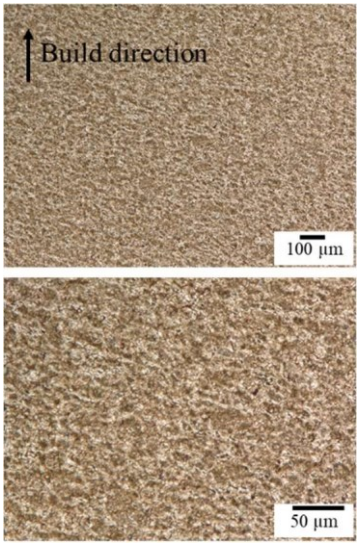

Fig. 11. Individual images for zones in overlap region (tracks 1 and 2): location C, track 1 deposit from Fig. 7.

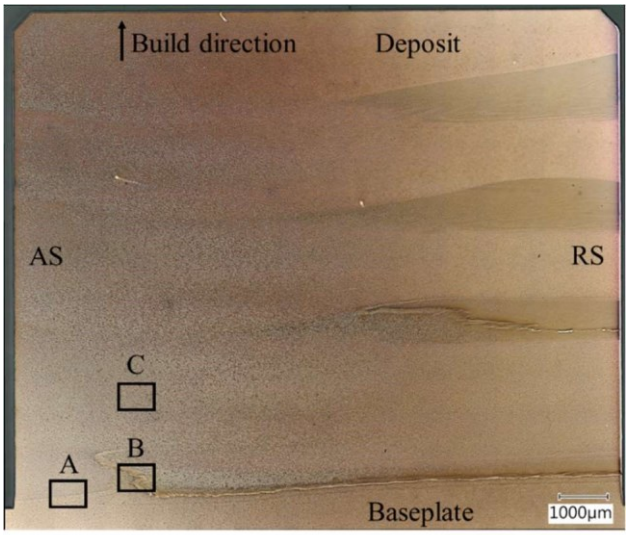

Fig. 12. Standalone region (track 1) microstructure.

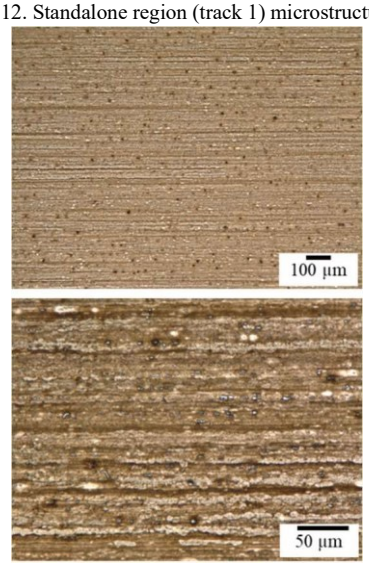

Fig. 13. Individual images for zones in standalone region (track 1): baseplate.

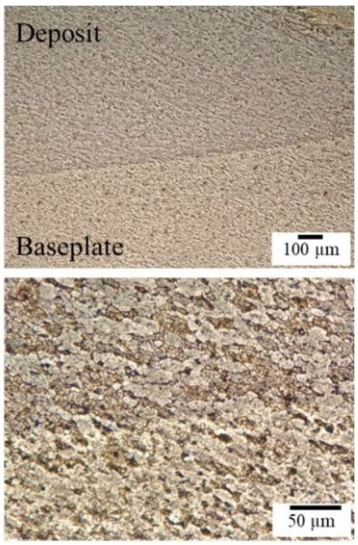

Fig. 14. Individual images for zones in standalone region (track 1): location A, interface from Fig. 12.

4. Conclusions

This paper described the combination of AFSD, structured light scanning, and CNC machining in a hybrid manufacturing scenario. The demonstration part was an aluminum aerospace flight panel, although the material and application are not limited to this domain. The AFSD material demonstrated machinability similar to wrought aluminum. The structured light scanning procedure provided an accurate stock model for the CAM software, while also ensuring the desired part geometry was contained within the printed preform. Tool tip FRF measurements enabled the selection of optimal machining parameters. Post-process measurements were used to compare the final part with the intended CAD design and evaluate the microstructure of the baseplate and deposited material. Ultimately, this work demonstrated a hybrid manufacturing approach that leverages AFSD, metrology, and machining to provide a new option for the production of aerospace flight panels, as well as other metallic components traditionally obtained from wrought plate, castings, or forgings.

Future work will focus on predictive modeling to describe deposition outcomes (microstructure and mechanical properties) as a function of AFSD operating parameters, deposition material (i.e., the wrought stock), and postdeposition heat treating. Given this modeling approach, a digital twin for hybrid manufacturing by AFSD, structured light scanning, and CNC machining will advance capabilities for both defense and commercial applications.

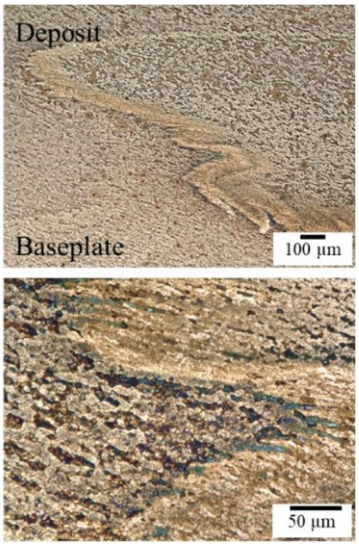

Fig. 15. Individual images for zones in standalone region (track 1): location B, interface from Fig. 12.

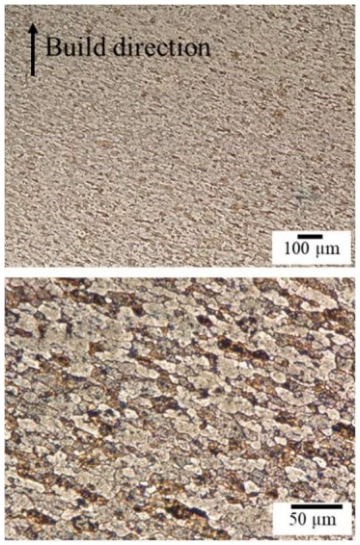

Fig. 16. Individual images for zones in standalone region (track 1): location C, deposit from Fig. 12.

Acknowledgements

This work was partially supported by the DOE Office of Energy Efficiency and Renewable Energy (EERE), Advanced Manufacturing Office (AMO), under contract DE-AC0500OR22725. The US government retains and the publisher, by accepting the article for publication, acknowledges that the US government retains a nonexclusive, paid-up, irrevocable, worldwide license to publish or reproduce the published form of this manuscript, or allow others to do so, for US government purposes. DOE will provide public access to these results of federally sponsored research in accordance with the DOE Public Access Plan (http://energy.gov/downloads/doe-publicaccess-plan). The authors would also like to acknowledge support from the NSF Engineering Research Center for Hybrid Autonomous Manufacturing Moving from Evolution to Revolution (ERC-HAMMER) under Award Number EEC2133630.

References

[1] Dehoff, R.R., Kirka, M.M., Sames, W.J., Bilheux, H., Tremsin, A.S., Lowe, L.E. and Babu, S.S., 2015. Site specific control of crystallographic grain orientation through electron beam additive manufacturing. Materials Science and Technology, 31(8), pp.931938.

[2] Hang, Z.Y., Jones, M.E., Brady, G.W., Griffiths, R.J., Garcia, D., Rauch, H.A., Cox, C.D. and Hardwick, N., 2018. Non-beam-based metal additive manufacturing enabled by additive friction stir deposition. Scripta Materialia, 153, pp.122-130.

[3] Khodabakhshi, F. and Gerlich, A.P., 2018. Potentials and strategies of solid-state additive friction-stir manufacturing technology: A critical review. Journal of Manufacturing Processes, 36, pp.77-92.

[4] Yu, H.Z. and Mishra, R.S., 2021. Additive friction stir deposition: a deformation processing route to metal additive manufacturing. Materials Research Letters, 9(2), pp.71-83.

[5] Gopan, V., Wins, K.L.D. and Surendran, A., 2021. Innovative potential of additive friction stir deposition among current laser based metal additive manufacturing processes: A review. CIRP Journal of Manufacturing Science and Technology, 32, pp.228-248.

[6] Priedeman, J.L., Phillips, B.J., Lopez, J.J., Tucker Roper, B.E., Hornbuckle, B.C., Darling, K.A., Jordon, J.B., Allison, P.G. and Thompson, G.B., 2020. Microstructure development in additive friction stir-deposited Cu. Metals, 10(11), p.1538.

[7] Perry, M.E., Griffiths, R.J., Garcia, D., Sietins, J.M., Zhu, Y. and Hang, Z.Y., 2020. Morphological and microstructural investigation of the non-planar interface formed in solid-state metal additive manufacturing by additive friction stir deposition. Additive Manufacturing, 35, p.101293.

[8] Griffiths, R.J., Garcia, D., Song, J., Vasudevan, V.K., Steiner, M.A., Cai, W. and Hang, Z.Y., 2021. Solid-state additive manufacturing of aluminum and copper using additive friction stir deposition: Process-microstructure linkages. Materialia, 15, p.100967.

[9] Agrawal, P., Haridas, R.S., Yadav, S., Thapliyal, S., Gaddam, S., Verma, R. and Mishra, R.S., 2021. Processing-structure-property correlation in additive friction stir deposited Ti-6Al-4V alloy from recycled metal chips. Additive Manufacturing, 47, p.102259.

[10] Phillips, B.J., Mason, C.J.T., Beck, S.C., Avery, D.Z., Doherty, K.J., Allison, P.G. and Jordon, J.B., 2021. Effect of parallel deposition path and interface material flow on resulting microstructure and tensile behavior of Al-Mg-Si alloy fabricated by additive friction stir deposition. Journal of Materials Processing Technology, 295, p.117169.

[11] Perry, M.E., Rauch, H.A., Griffiths, R.J., Garcia, D., Sietins, J.M., Zhu, Y., Zhu, Y. and Hang, Z.Y., 2021. Tracing plastic deformation path and concurrent grain refinement during additive friction stir deposition. Materialia, 18, p.101159.

[12] Williams, M.B., Robinson, T.W., Williamson, C.J., Kinser, R.P., Ashmore, N.A., Allison, P.G. and Jordon, J.B., 2021. Elucidating the effect of additive friction stir deposition on the resulting microstructure and mechanical properties of magnesium alloy we43. Metals, 11(11), p.1739.

[13] Mukhopadhyay, A. and Saha, P., 2022. A critical review on process metrics–microstructural evolution–process performance correlation in additive friction stir deposition (AFS-D). Journal of the Brazilian Society of Mechanical Sciences and Engineering, 44(9), pp.1-35.

[14] Joshi, S.S., Sharma, S., Radhakrishnan, M., Pantawane, M.V., Patil, S.M., Jin, Y., Yang, T., Riley, D.A., Banerjee, R. and Dahotre, N.B., 2022. A multi modal approach to microstructure evolution and mechanical response of additive friction stir deposited AZ31B Mg alloy. Scientific Reports, 12(1), pp.1-15.

[15] Zeng, C., Ghadimi, H., Ding, H., Nemati, S., Garbie, A., Raush, J. and Guo, S., 2022. Microstructure Evolution of Al6061 Alloy Made by Additive Friction Stir Deposition. Materials, 15(10), p.3676.

[16] Phillips, B.J., Avery, D.Z., Liu, T., Rodriguez, O.L., Mason, C.J.T., Jordon, J.B., Brewer, L.N. and Allison, P.G., 2019. Microstructuredeformation relationship of additive friction stir-deposition Al– Mg–Si. Materialia, 7, p.100387.

[17] Alzahrani, B., El-Sayed Seleman, M.M., Ahmed, M.M., Elfishawy, E., Ahmed, A.M., Touileb, K., Jouini, N. and Habba, M.I., 2021. The Applicability of Die Cast A356 Alloy to Additive Friction Stir Deposition at Various Feeding Speeds. Materials, 14(20), p.6018.

[18] Joshi, S.S., Patil, S.M., Mazumder, S., Sharma, S., Riley, D.A., Dowden, S., Banerjee, R. and Dahotre, N.B., 2022. Additive friction stir deposition of AZ31B magnesium alloy. Journal of Magnesium and Alloys.

[19] Garcia, D., Hartley, W.D., Rauch, H.A., Griffiths, R.J., Wang, R., Kong, Z.J., Zhu, Y. and Hang, Z.Y., 2020. In situ investigation into temperature evolution and heat generation during additive friction stir deposition: A comparative study of Cu and Al-Mg-Si. Additive Manufacturing, 34, p.101386.

[20] Beladi, H., Farabi, E., Hodgson, P.D., Barnett, M.R., Rohrer, G.S. and Fabijanic, D., 2022. Microstructure evolution of 316L stainless steel during solid-state additive friction stir deposition. Philosophical Magazine, 102(7), pp.618-633.

[21] Griffiths, R.J., Petersen, D.T., Garcia, D. and Yu, H.Z., 2019. Additive friction stir-enabled solid-state additive manufacturing for the repair of 7075 aluminum alloy. Applied Sciences, 9(17), p.3486.

[22] Hartley, W.D., Garcia, D., Yoder, J.K., Poczatek, E., Forsmark, J.H., Luckey, S.G., Dillard, D.A. and Hang, Z.Y., 2021. Solid-state cladding on thin automotive sheet metals enabled by additive friction stir deposition. Journal of Materials Processing Technology, 291, p.117045.

[23] Avery, D.Z., Cleek, C.E., Phillips, B.J., Rekha, M.Y., Kinser, R.P., Rao, H.M., Brewer, L.N., Allison, P.G. and Jordon, J.B., 2022. Evaluation of Microstructure and Mechanical Properties of Al-ZnMg-Cu Alloy Repaired via Additive Friction Stir Deposition. Journal of Engineering Materials and Technology, 144(3), p.031003.

[24] Peter Martin, L., Luccitti, A. and Walluk, M., 2022. Evaluation of Additive Friction Stir Deposition for the Repair of Cast Al-1.4 Si1.1 Cu-1.5 Mg-2.1 Zn. Journal of Manufacturing Science and Engineering, 144(6).

[25] Ahmed, M.M., El-Sayed Seleman, M.M., Elfishawy, E., Alzahrani, B., Touileb, K. and Habba, M.I., 2021. The effect of temper condition and feeding speed on the additive manufacturing of AA2011 parts using friction stir deposition. Materials, 14(21), p.6396.

[26] Anderson-Wedge, K., Avery, D.Z., Daniewicz, S.R., Sowards, J.W., Allison, P.G., Jordon, J.B. and Amaro, R.L., 2021. Characterization of the fatigue behavior of additive friction stirdeposition AA2219. International Journal of Fatigue, 142, p.105951.

[27] Stubblefield, G.G., Fraser, K., Phillips, B.J., Jordon, J.B. and Allison, P.G., 2021. A meshfree computational framework for the numerical simulation of the solid-state additive manufacturing process, additive friction stir-deposition (AFS-D). Materials & Design, 202, p.109514.

[28] Merritt, G.R., Williams, M.B., Allison, P.G., Jordon, J.B., Rushing, T.W. and Cousin, C.A., 2022. Closed-Loop Temperature and Force Control of Additive Friction Stir Deposition. Journal of Manufacturing and Materials Processing, 6(5), p.92.

[29] Schmitz, T. and Smith, K.S., 2019. Machining Dynamics: Frequency Response to Improved Productivity, Second Edition, Springer, New York, NY.

[30] Kim, H.S. and Schmitz, T.L., 2007. Bivariate uncertainty analysis for impact testing. Measurement Science and Technology, 18(11), p.3565.

[31] Cornelius, A., Dvorak, J., Jacobs, L., Penney, J. and Schmitz, T., 2021. Combination of structured light scanning and external fiducials for coordinate system transfer in hybrid manufacturing. Journal of Manufacturing Processes, 68, pp.1824-1836.

[32] Dvorak, J., Cornelius, A., Corson, G., Zameroski, R., Jacobs, L., Penney, J. and Schmitz, T., 2022. A machining digital twin for hybrid manufacturing. Manufacturing Letters, 33, pp.786-793.

[33] Cornelius, A., Jacobs, L., Lamsey, M., McNeil, L., Hamel, W. and Schmitz, T., 2022. Hybrid manufacturing of Invar mold for carbon fiber layup using structured light scanning. Manufacturing Letters, 33, pp.133-142.

[34] Jacobs, L. and Schmitz, T., 2022, Repeatability and reproducibility studies for structured light scanning, American Society for Precision Engineering Annual Meeting, November 1-5, Minneapolis, MN.